Solar Energy Materials & Solar Cells 138 (2015) 9–16

Contents lists available at ScienceDirect

Solar Energy Materials & Solar Cells

journal homepage: www.elsevier.com/locate/solmat

Sn-deficiency in the electrodeposited ternary $Cu_xSn_yS_z$ thin films by ECALE

Stefano Caporali [a,d,*], Alexander Tolstogouzov [b,c], Orlando M.N.D. Teodoro [b], Massimo Innocenti [a], Francesco Di Benedetto [d,e], Serena Cinotti [a], Rosaria Anna Picca [f], Maria Chiara Sportelli [f], Nicola Cioffi [f]

[a] Dipartimento di Chimica, Università di Firenze, via della Lastruccia 3, 50019 Sesto Fiorentino (FI), Italy
[b] Centre for Physics and Technological Research (CeFITec), Department de Física da Faculdade de Ciências Tecnologia (FCT), Universidade Nova de Lisboa, Campus de Caparica, 2829-516 Caparica, Portugal
[c] Ryazan State Radio Engineering University, Gagarin street, 59/1, 390005 Ryazan, Russian Federation
[d] Consorzio INSTM, via Giusti 9, 50123 Firenze, Italy
[e] Dipartimento di Scienze della Terra, Università degli Studi di Firenze, 50120 Firenze, Italy
[f] Dipartimento di Chimica, Università degli Studi di Bari, via Orabona 4, 70126 Bari, Italy

ARTICLE INFO

Article history:
Received 27 November 2014
Received in revised form
10 February 2015
Accepted 23 February 2015
Available online 12 March 2015

Keywords:
Electrodeposition
Cu/Sn chalcogenides
CTS
PAR-XPS
ECALE
TOF-SIMS.

ABSTRACT

Ternary $Cu_xSn_yS_z$ thin films with different Cu/Sn atomic ratios and thicknesses have been electrochemically deposited on the (111) face of a silver single crystal. The surface morphology and chemical composition of these chalcogenides, which have attracted considerable worldwide interest as low cost high conversion efficiency photovoltaic devices, have been characterized by means of SEM, parallel angle resolved (PAR-XPS) and TOF-SIMS depth profiling in order to gain insight into the morphology and element distribution within the layer and their effect on the band gap.

This study constitutes the first in-depth chemical study on $Cu_xSn_yS_z$ thin films, providing evidence of notable discrepancies between the expected and real composition, especially regarding the Cu/Sn ratio. The samples were found to be chemically homogeneous through the whole deposit even though strongly tin depleted regardless their thickness or deposition sequence. Finally, the literature band gap data were discussed on the basis of these findings.

1. Introduction

The progress in thin film solar cell technology represents one of the main technological breakthroughs for the development of a planet-scale economy based on renewable energy and the replacement of fossil fuels as supply of primary energy. Nevertheless, for such thin film solar cell technology to become viable, the development of low-cost deposition methods is essential. In fact, not only do we need materials with high energy-conversion properties, but it is also vital that large amounts of these materials are available to allow the mass production of cheap and efficient devices. The energetic and environmental costs of these devices must be considered in terms of their whole life-cycle. Hence, the device production, as well as their end-of-life issues, as recycling/disposal methodologies, must be rigorously taken into account. In the light of these considerations, devices based upon rare (indium, gallium, germanium, tellurium) or toxic (selenium, cadmium) elements must be avoided in all layers of new thin film solar devices [1–3].

The industrial interest is therefore moving towards the realization of cost-effective thin film solar cells based on relatively common, inexpensive and non-toxic elements. In this context, ternary (kuramite, Cu_3SnS_4) and quaternary (stannite, Cu_2FeSnS_4, and kesterite, Cu_2ZnSnS_4 or CZTS) chalcogenides are attracting increasing interest from researchers worldwide, due to their good performance based on relatively simple chemistry and the absence of significant economic or environmental concerns related to their production, use and disposal [4–6]. Multinary chalcogenides are usually synthesized by using high temperature and/or vacuum techniques. To further improve the competitiveness of these materials, viable routes that avoid the need of expensive high vacuum techniques, without loosing conversion efficiency, are being actively investigated [7,8].

Although, to date, there have been only a few reports regarding the preparation of CZTS solar cells entirely via non-vacuum

* Corresponding author at: Università degli Studi di Firenze, via della Lastruccia 3-13, 50019 Sesto Fiorentino, Italy. Tel.: +39 055 4573146.
E-mail address: stefano.caporali@unifi.it (S. Caporali).

http://dx.doi.org/10.1016/j.solmat.2015.02.029
0927-0248/

techniques [8–10], the use of facile and scalable techniques is a mandatory step to further improve the competitiveness of thin film modules for photovoltaic applications [10–12]. Among the non-vacuum techniques, electrodeposition [13–15] and, especially, ECALE (Electrochemical Atomic Layer Epitaxy) represent the most promising alternative routes to deposit ternary chalcogenides [16]. The formation of a monolayer of the compound by ECALE consists of the alternating underpotential deposition of the metallic element and the underpotential deposition of the non-metallic element. The redox potential, pH and reactants can be adjusted to optimize the deposition process. In this perspective, the ECALE technique is a valid approach for the attainment of II–VI [17–20], III–V [21–23] compounds, as well as ternary and quaternary semiconductors on conductive substrates [24,25].

Clearly, the characteristics of the deposits change as a function of the deposition conditions, the number of cycles and the chemical composition. Since these differences can affect the optoelectronic properties, an in-depth knowledge of the physicochemical and morphological characteristics is mandatory for the optimization of these materials and their development for the mass production of photovoltaic devices.

In this study, we provide a detailed morphological and chemical description of ECALE-deposited $Cu_xSn_yS_z$ thin films characterized by different thicknesses and nominal Cu/Sn ratio highlighting, for the first time, considerable differences between the nominal and real composition of the compounds.

2. Materials and experimental setup

2.1. Sample preparation

The ternary compounds were prepared alternating the underpotential deposition of sulfur with that of copper and tin on Ag (111) [26]. A sketch depicting the underpotential deposition of ternary sulfides is illustrated in Fig. 1.

In principle, the stoichiometry of the electrodeposited ternary sulfide can be tuned using different deposition sequences, i.e. combining different numbers of ECALE cycles of each binary compound. In the same way, the thickness of the deposit can be controlled as a function of the number of cycles used, making this electrochemical approach very versatile. In this study, following the procedure previously described [26], two sets of $Cu_xSn_yS_z$ thin films were prepared and investigated; a thinner deposit, 10 cycles (S/Sn/S/Cu; 20 sulfur atomic layers) with a Cu/Sn=1 nominal ratio named sample #1 and a thicker one, twenty cycles (S/Sn/S/Cu/S/Sn; 60 sulfur atomic layers) with double the amount of tin, Cu/Sn=0.5 nominal ratio named sample #2. Table 1 resumes the details of both samples.

2.2. Characterization methods

Sample morphology and uniformity were determined by a Scanning Electron Microscope (SEM; Hitachi S-2300) operating at 20 kV.

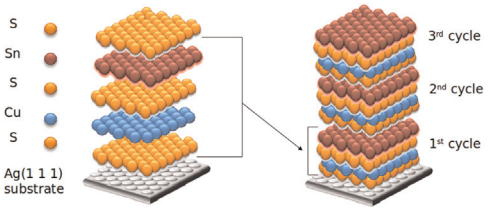

Fig. 1. Schematic representation of ternary compound thin film growth by means of alternating electrodeposition of S, Cu and Sn layers.

Table 1
Type of Ag/S/((Cu/S)k(Sn/S)j)n samples prepared.

Sample	Expected Cu/Sn ratio	Number of deposition cycles (n)	Number of sulfur layers
Sample #1 ($k=1$; $j=1$)	1	10	20
Sample #2 ($k=1$; $j=2$)	0.5	20	60

Near-surface chemical composition was obtained by means of X-ray Photoelectron Spectroscopy (XPS) measurements performed in an ultra-high vacuum system. Conventional XPS analyzes were performed using a VSW HAC 5000 hemispherical electron energy analyzer and a non-monochromatized Mg-Kα X-ray source (1253.6 eV). The source power was 100 W (10 kV × 10 mA) and the spectra were acquired in the constant analyzer energy mode (CAE) at pass energy $E_{pas}=44$ eV. The overall energy resolution was 1.2 eV, as full-width at half-maximum (FWHM), for the Ag $3d_{5/2}$ line of a pure silver reference. The recorded spectra were fitted using CasaXPS software employing Gauss–Lorentz curves after subtraction of a Shirley-type background.

The samples were introduced in the UHV system via a loadlock under an inert gas (N_2) flux, in order to minimize the exposure to air contaminants, and kept in the introduction chamber for at least 12 h before the measurements. Ion sputtering was performed using an argon beam (chamber pressure 10^{-7} mbar) at 2 kV and 20 mA current.

Parallel angle resolved XPS (PAR-XPS) analyzes were carried out using a Thermo Fisher Scientific Theta Probe Spectrometer equipped with a monochromatic AlKα source (beam spot diameter 300 μm) operating in CAE mode. Samples were not sputtered before analysis. Survey and high-resolution spectra (C1s, O1s, Ag3d, Cu2p, Sn3d, S2p, Cl2p, Na1s, Ag $M_{4,5}N_{45}N_{45}$, Cu $L_3M_{45}M_{45}$) were acquired at E_{pas} of 150 and 100 eV, respectively, and with a step size of 1.0 and 0.1 eV, respectively.

Six emission angles (θ, angle measured with respect to the sample surface normal) were selected between 28° ("bulk" angle) and 78° ("surface" angle) with a 10° step, to collect angle resolved XP spectra. The overall acquisition time was kept well below 1 h per sampled point, as a good compromise between acceptable signal-to-noise ratio and prevention from X-ray artefacts. At least three sampling points were averaged to evaluate the surface chemical composition. No changes in the lineshape were observed within the analysis run time, as assessed by repetitive spectra acquisitions at regular intervals during the experiment. Binding Energy (BE) scale was calibrated taking as reference the position of aliphatic C1s component (adventitious carbon) at 284.8 ± 0.1 eV. Curve-fit and element quantification were performed processing high-resolution XP spectra by Thermo Avantage software (v. 4.75, © 1999–2010).

TOF-SIMS depth profiling was achieved measuring positive secondary ion spectra in the mass range of 0.5–400 m/z using an upgraded VG Ionex IX23LS TOF-SIMS [27,28]. A focused liquid–metal Ga^+ gun MIG 300PB in the pulsed mode (6 kHz/40 ns) was employed as a source of probing ions. A beam current in the continuous mode at 14 keV of the primary energy was 15–20 nA. During analysis the Ga^+ beam was scanned over an area of 220 μm × 140 μm (10 kHz, 128 × 128 pixels). Data acquisition time was 60 s; the sample potential was +5 kV (the impact energy of the analysis ions was 9 keV).

Sputter depth profiling was carried out in the dual beam mode using a duoplasmatron DP50B as a sputter ion source of O_2^+ ions with 8 keV bombarding energy (samples were grounded during the sputtering cycle). The sample current was ca. 100–120 nA, raster size ca. 1 mm^2 (10 kHz, 128 × 128 pixels), and the time of

sputtering for every cycle 30–60 s. The analysis and sputter ion beams are interlaced in the course of depth profiling.

3. Results and discussion

3.1. SEM analysis

Figs. 2 and 3 show images of the two investigated samples. Sample #1 ($k=1$, $j=1$, 10 cycles, 20 sulfur atomic layers) has a rough surface characterized by a large number of holes, in the range of 50–200 nm. Sample #2 ($k=1$, $j=2$, 20 cycles, 60 sulfur atomic layers) appears much smoother and compact, even if sub-micron size pores are still clearly detectable.

As previously observed [26], the morphology of the coating, except for the holes, closely resembles that of the silver substrate. It is likely that the holes are a consequence of a structural rearrangement of the thin film that takes place just after the deposition of the very first atomic layers. The preparation of a deposit with a large number of layers contributes to the filling of the holes, resulting in a denser and more compact deposit as depicted in Fig. 3.

3.2. X-ray photoelectron spectroscopy analysis

The XPS technique was employed to assess the chemical composition of the very near surface portion of the thin films, due to its high surface sensitivity and chemical speciation capability. High-resolution regions relevant to Cu2p, S2p, Sn3d, and Cu $L_3M_{45}M_{45}$ transitions were investigated to identify the most probable surface chemical environments.

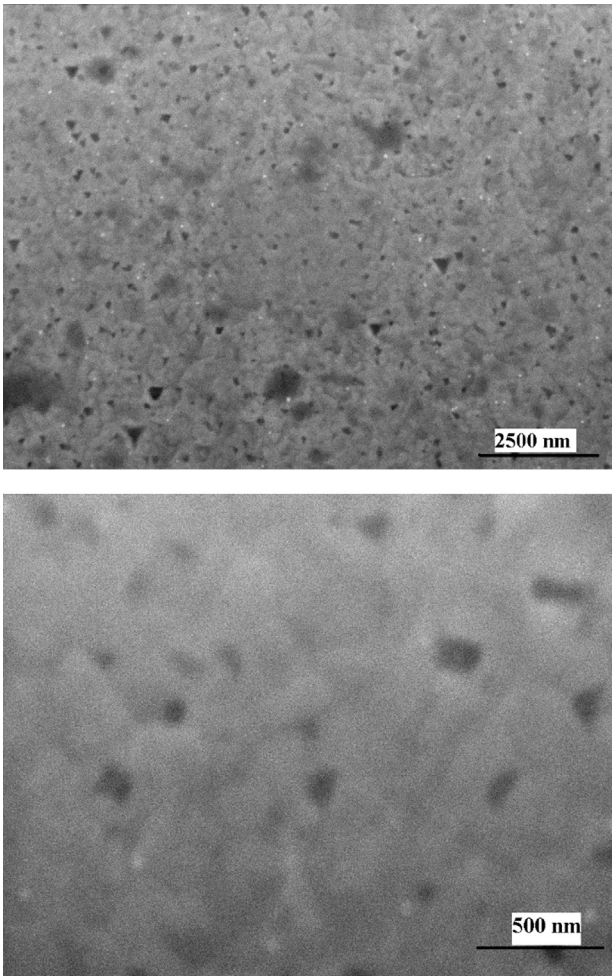

Fig. 2. SEM images at different magnifications of sample#1 ($k=1$, $j=1$, 10 cycles, 20 sulfur layers).

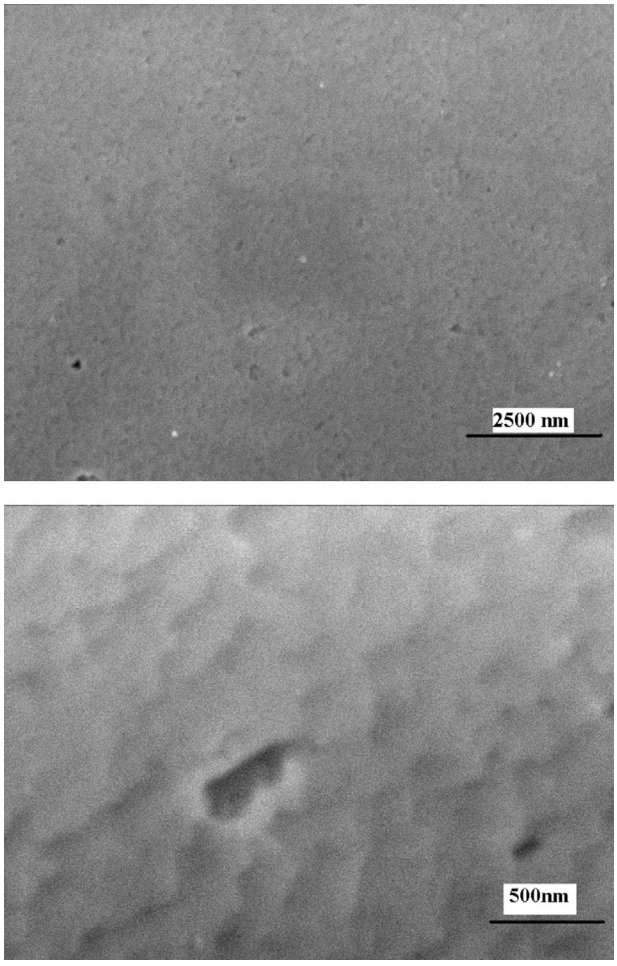

Fig. 3. SEM images at different magnifications of sample#2 ($k=1$, $j=2$, 20 cycles, 60 sulfur layers).

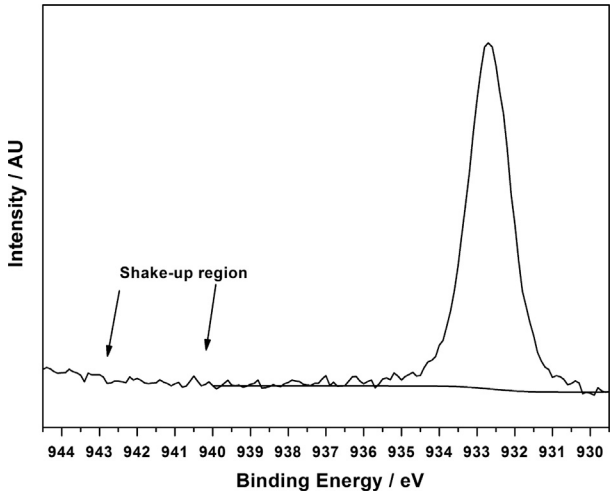

Fig. 4. Typical Cu2p$_{3/2}$ XPS spectrum of $Cu_xSn_yS_z$ samples. The arrows highlight the absence of shake-up features in the indicated frequency region, which are markers of the presence of Cu(II) compounds.

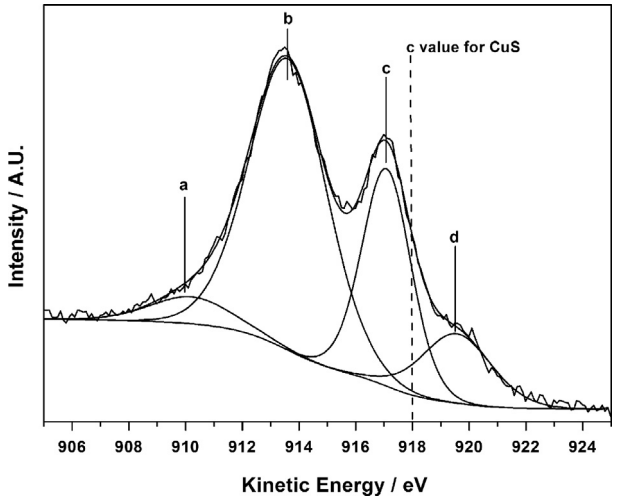

Fig. 5. Typical Cu $L_3M_{45}M_{45}$ spectrum of $Cu_xSn_yS_z$ samples. The dotted line indicates the KE value expected for peak c in the case of CuS specie.

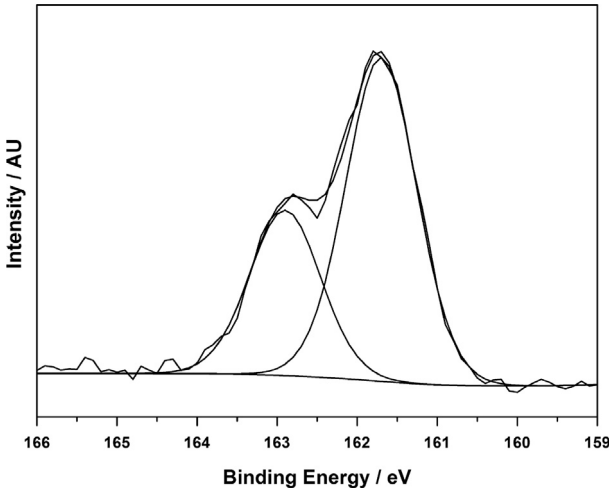

Fig. 6. Typical S2p spectrum of $Cu_xSn_yS_z$ samples.

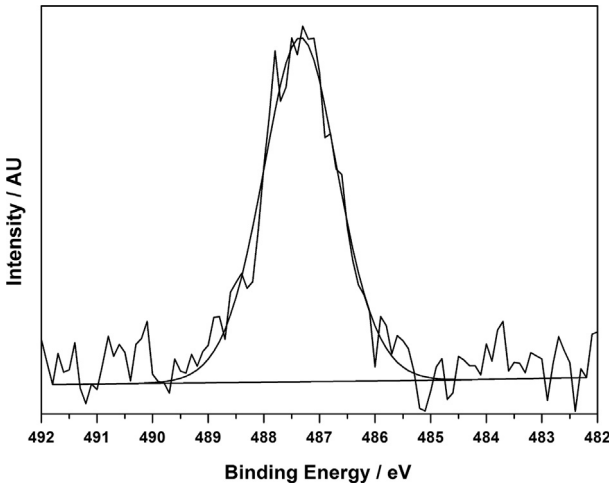

Fig. 7. Typical $Sn3d_{5/2}$ spectrum of $Cu_xSn_yS_z$ samples.

The Cu2p core transition is characterized by a doublet due to the spin–orbit coupling, producing the $2p_{3/2}$ and $2p_{1/2}$ components. A typical $Cu2p_{3/2}$ XP spectrum of the studied films is reported in Fig. 4, showing only a single peak at BE = 932.7 ± 0.1 eV, which was attributed to Cu(I) [29,30]. Several observations support this conclusion. The peak is narrow (FWHM = 1.4 eV), compared to the broader signals associated with Cu(II). Moreover, the presence of a Cu(II) species can be ruled out as no shake-up signals (typical labels of this valence status) are detected at BE values around 940–945 eV [29].

Cu surface chemical speciation in the electrodeposited materials was further investigated by analyzing the Cu $L_3M_{45}M_{45}$ Auger transition. Several fundamental studies have provided insight into the peaks composing the overall Cu Auger spectrum [31–35]. On this basis, four components (a–d) were identified in the deconvoluted spectrum of Fig. 5. The narrow peak c was attributed to the ^3P, ^1G, ^1D triad, falling at Kinetic Energy (KE) = 917.1 ± 0.2 eV. Peak d (KE = 919.6 ± 0.2 eV) was unambiguously assigned to ^3F line. On the other hand, in the region at lower KE values, the assignment of the peaks labeled a (KE = 910.2 ± 0.3 eV) and b (KE = 913.6 ± 0.1 eV), is less clear. In fact, the observed shape, intensity, and positions associated with these components are not only due to the main transition–as defined by the process itself–and to line ^1S in particular, but also to Auger vacancy satellites arising from spectator vacancies in the M_{45} subshell [33], Coster–Kronig transitions [33,35], and static extra-atomic relaxation effects [34]. A more extensive explanation of these spectral details is beyond the scope of this work, since for chemical speciation purposes, the most useful component of the Cu $L_3M_{45}M_{45}$ Auger spectrum is by far peak c.

In our study, the position of peak c agrees well with what expected for Cu_2S [30], whereas, in the case of CuS species, the homologous Cu $L_3M_{45}M_{45}$ (^1G) component should be found at much higher values (KE = 918.0 ± 0.2 eV) [36] (see the dotted line in Fig. 5).

The maximum of peak c is also typically employed for the calculation of the so-called modified Auger parameter ($\alpha' = BE_{Cu2p3/2} + KE_{CuLMM}$) [37]. For our samples, the calculated α' parameter was 1849.8 ± 0.3 eV, which again is in good agreement with that reported for Cu_2S [30].

The S2p region showed a single doublet (Fig. 6), which was fitted by two peaks at BE values of 161.7 ± 0.1 eV and 162.9 ± 0.1 eV, corresponding to $2p_{3/2}$ and $2p_{1/2}$ components, respectively. Although these values agree with the literature data for inorganic sulfides [30,38,39], a further calculation was performed to confirm the assignments deriving from copper signals. In particular, the separation between the $S2p_{3/2}$ and $Cu2p_{3/2}$ transitions ($\Delta ECu2p_{3/2}–S2p_{3/2}$) is a diagnostic parameter for the discrimination between Cu_2S and CuS species. In our study, it was equal to 771.0 ± 0.2 eV, which is again in agreement with the reported value of 770.9 eV for Cu_2S [30], thus further confirming that copper is almost exclusively present as Cu(I) sulfide.

Finally, the absence of other sulfur peaks at higher BE, which are associated with oxidized sulfur species, indicates a good stability of the electrodeposited films towards air-induced oxidation.

Unexpectedly, the Sn3d region was significantly less intense than the copper signals, revealing a different surface composition from that hypothesized from Table 1. Despite its low intensity, a doublet was identified in this region, with a main component $Sn3d_{5/2}$ at BE = 487.3 ± 0.2 eV, possibly compatible with the Sn(IV) state [36] (Fig. 7).

A detailed analysis of the surface elemental abundance of Cu, Sn, S and Ag is given in Table 2, where elemental ratios are compared. Differences between samples as well as differences from nominal and experimental values are apparently outlined. For both samples, the amount of tin is well below that inferred from the deposition sequence (i.e. less than 1/10). This confirms a result by Loglio et al. [40], according to which different metals can exhibit very different growth rates per single deposition cycle. Previous electrochemical measurements pointed out that the total charge involved in the stripping of metals, considered as copper and tin together, as well as that associated with sulfur, is a linear function of the number of layers [26]. However, in that study the Cu/Sn ratio was not determined, as there is no electrochemical way to

Table 2
Atomic ratios of the near surface portion of the samples.

Sample	Atomic ratio		
	Cu/Sn	Cu/S	Cu/Ag
Sample #1 (nominal Cu/Sn ratio=1)	13 ± 3	1.38 ± 0.15	0.21 ± 0.01
Sample #2 (nominal Cu/Sn ratio=0.5)	9 ± 4	1.3 ± 0.3	0.26 ± 0.01

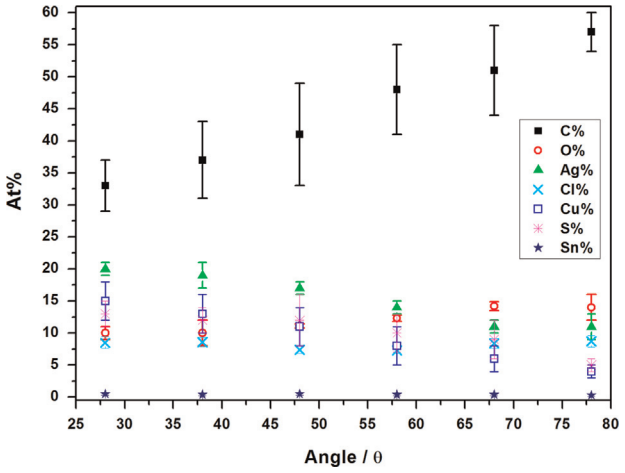

Fig. 8. Parallel angle resolved XPS elemental analysis of sample #2 ($k=1$, $j=2$, 20 cycles, 60 sulfur layers), showing the dependence of the surface chemical composition upon the emission angle θ. From left to right, the ratio between the sampled thickness d and its maximum value d_{max} (relevant to $\theta = 0°$) changes from 0.88 to 0.20.

distinguish between the two elements during the stripping procedure.

PAR-XPS investigation was performed to further investigate the Cu/Sn ratio in the inner surface layers of the samples. Such an approach allows a non-destructive investigation of concentration depth profiles. In this experiment, low values of the emission angle (θ) account for "bulk" sensitive angles, while high values correspond to "surface" sensitive data. The chemical composition of the analyzed films was evaluated at each sampling angle in terms of atomic per cent (At%) of the identified elements. Fig. 8 shows the PAR–XPS results obtained on sample #2 ($k=1$, $j=2$, 20 cycles). As expected for an air-exposed sample, which was not sputter-cleaned before analysis, carbon was the most abundant element at each angle. Its increased abundance in the outer surface layers (higher θ values) was accompanied by a slight increase of the oxygen content, thus confirming the presence of oxygenated carbon contamination.

Concerning to the Cu/Sn ratio, the experiment revealed that the observed lack of tin is not due to copper enrichment at the surface, but that it involves most of the deposited thickness. A similar result was also observed in spectra collected after Ar sputtering (data not shown), confirming copper enrichment throughout the entire sample thickness.

Silver belonging to the substrate was detected at all angles, though a remarkable decrease was observed when decreasing the sampled depth. Such a trend is attributed to the intrinsic porous nature of the analyzed films (see Figs. 2, 3).

A significant amount of chlorine was also observed, that did not vary with the sampled depth. The homogeneous distribution of this element throughout the entire thickness of the deposit could be attributable to the adsorption of Cl^- ions during the growth of the deposit. Indeed, chlorides are present in the electrodeposition medium as supporting electrolyte. Fig. 9 provides a detailed view

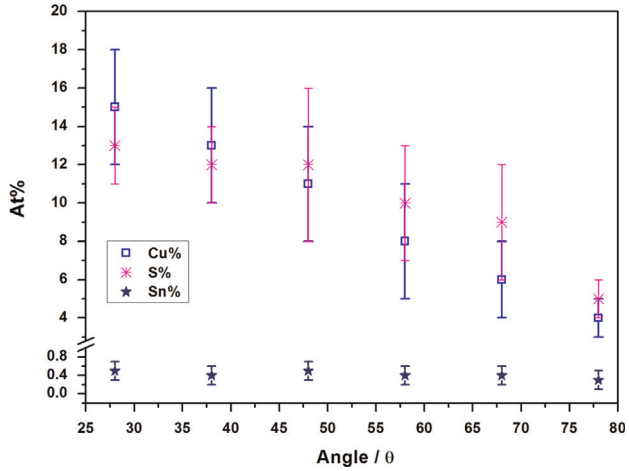

Fig. 9. Selected trends from Fig. 8, outlining the depth dependence of Cu, S, and Sn atomic percentages relevant to sample #2 ($k=1$, $j=2$, 20 cycles, 60 sulfur layers).

of the in-depth distribution of specific elements of the electrodeposited material such as copper, sulfur, and tin.

The percentages of copper and sulfur seem to be strictly correlated, showing a similar decrease when the outer surface layers are sampled (e.g. upon increasing the emission angle). On the other hand, the tin content is apparently invariant with depth, at least within the high uncertainty limits associated.

It is important to recall when considering the whole ternary Cu–Sn–S system [41] that the metal-to-sulfur ratio and the ratio between the two metals in these ternary compounds can exhibit a very high degree of variability. Two extreme situations can be considered: Cu_5SnS_4, where metal/S=1.5 and Cu/Sn=5, and $Cu_2Sn_{3.75}S_8$, where metal/S=0.71875 and Cu/Sn=0.533. Accordingly, the experimental ratio Cu/Sn=10 revealed by the XPS analyses is not surprising. The chemical variability of the system, where many stable phases can account for minimal changes in the bulk composition of the compounds, allows the thin film to assume its own stoichiometry during the deposition cycles. Further structural investigation of the films will be made to ascertain whether they consist of one or more phases.

3.3. TOF-SIMS measurements

TOF-SIMS depth profiling was performed in order to better investigate the elemental composition throughout the film thickness. The depth distributions of the main positively charged secondary ion species, in a semilogarithmic scale, are presented in Fig. 10. It is evident that silver atoms are present on the surface of both samples, and with deeper penetration into the film structure the intensity of Ag^+ does not undergo significant changes. Nevertheless, complex molecular silver ions $Ag_2OH_2^+$ with 234 m/z and other similar clusters like Ag_2H^+, $(AgH)_2^+$, Ag_2OH^+, Ag_3H^+, etc. (not shown in Fig. 10) demonstrate an increase in the intensity versus the time of sputtering. These experimental trends are in a clear relationship with the porous structure of both films (Figs. 2 and 3). Silver ions originate mainly from the pores, and hydrogen-containing and hydrated silver clusters reflect the in-depth profile of the films.

The quantification of SIMS results is a very complex task, mainly due to the influence of the so-called matrix effect [42]. However, an approximate estimate of the atomic composition can be made using relative sensitivity factors

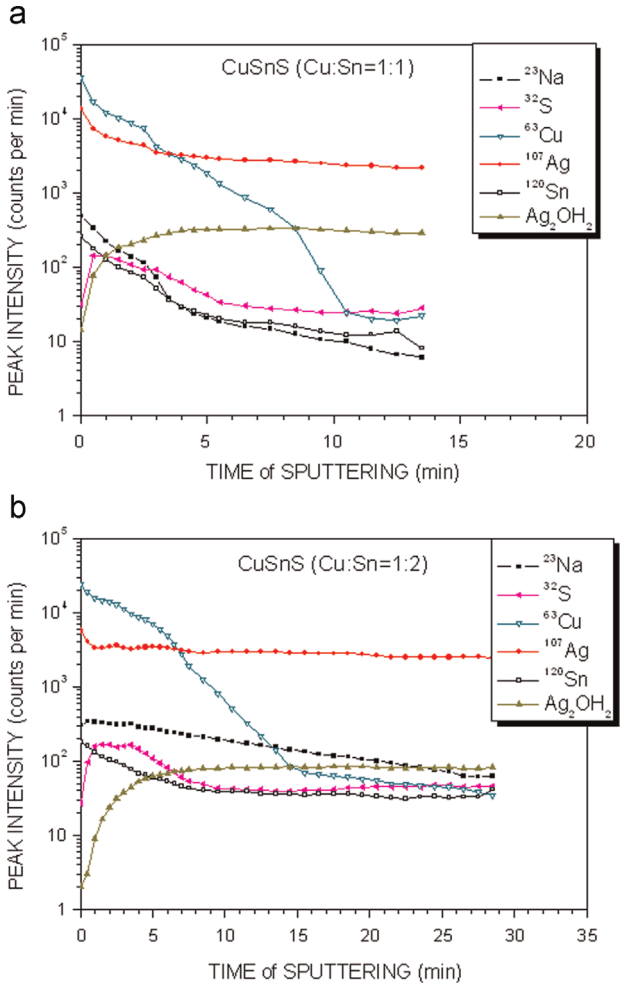

Fig. 10. Sputter depth profiles measured for samples #1 (a) and #2 (b).

$$C_i = \frac{(I \cdot \mathrm{RSF})_i}{\sum_i (I \cdot \mathrm{RSF})_i} \times 100\%, \quad (1)$$

where I is the experimentally measured peak intensity (sum of isotopes) of Cu, Sn, S, and Ag, and RSF is the relative sensitivity factor of these elements [43]. The literature values of the sensitivity factors for Cu, Sn, S, and Ag only in GaAs are reported in Table 3 [43]. Approximatively, for qualitative analisys purposes, these parameters can be considered valid also for sulphyde compound.

The experimental intensities of Cu^+, Sn^+, S^+, and Ag^+ secondary ion peaks (sum of all isotopes integrated within 0.5 m/z) for the 3rd point in Fig. 10 (after 60 s of the sputtering) are presented in Table 3. We calculated these values using the DECO computer code [43] for the accurate decomposition and identification of experimental mass spectra; the results of our estimate with Eq. (1) are listed in Table 3. An estimation of the depth of sputtering was achieved measuring the final crater depth (about 26 nm for sample #1 and about 50 nm for sample #2) and assuming a constant sputter rate. The thickness of the deposited films is estimated via the time of decrease of the sulfur signal to 50% of the maximal value; 4 min for sample #1 and 6 min for sample #2. This gives an estimate of the deposit thickness as 8 nm for sample #1 and 12 nm for sample #2.

Table 3
Intensities of the secondary ions (sum of all isotopes integrated within +/−0.5 m/z), SIMS relative sensitivity factors (for 8 keV O_2^+ primary ions) [33] and atomic concentration of the samples (calculated with the sensitivity factors for GaAs matrix).

Sample	Peak intensity, counts per min			
	Cu	Sn	S	Ag
Sample #1 (Cu/Sn=1)	8380	166	177	7560
Sample #2 (Cu/Sn=0.5)	15000	336	244	3390
RSF	Cu	Sn	S	Ag
	1	0.26	31.7	0.5
Sample	Atomic concentration, %			
	Cu	Sn	S	Ag
Sample #1 (Cu/Sn=1)	47.1	0.3	31.4	21.2
Sample #2 (Cu/Sn=0.5)	61.2	0.4	31.5	6.9

3.4. Considerations on the band gap value

The band-gap of these materials has been evaluated by diffuse reflectance spectroscopy measurements, and was found to vary as a function of the deposit thickness [26]: the highest band gap values (2.43 eV) were observed for the thinner layers ($k=1, j=1$, 10 cycles, sample #1), while lower values, down to 2.12 eV, were detected for the thicker deposits ($k=1, j=2$, 20 cycles, sample #2). The same authors [26] pointed out that the band gap value was only slightly affected by the nominal stoichiometry dictated by the cycle deposition sequence. This observation is now clearer: XPS and SIMS measurements, in fact, revealed that the deposits exhibit an almost constant Cu/Sn ratio with only a minor Sn-content. The experimental band gap values can be considered anomalously high if compared to SnS (1.5 eV) [44] or to Cu_2S (1.21 eV) [45]. Even though these values appear reasonable if compared to CuS (2.24 eV) [46] or SnS_2 (2.2–3.5 eV) [47], SIMS and especially XPS measurements ruled out the presence of these phases throughout the entire deposit thickness.

Taking into account the present XPS and SIMS results, we suggest that the presence of a ternary phase, where only a very low amount of Sn is hosted, is able to produce only a little reduction of the band gap values, respect to the typical $Cu_xSn_yS_z$ compounds (1.5–1.6 eV) [4,48]. It is well know how quantum size effects can modify the size of the band gap [49,50]. In the present case, in owe to extremely low thickness, it seems reasonable attribute the band gap reduction observed in sample #2 to the deposit increased thickness and improved homogeneity. On the basis of our results, increasing the amount of tin in the deposit would likely contribute to a decrease of the band gap to a greater extent than expected from previous studies.

4. Conclusions

Thin layers of $Cu_xSn_yS_z$ were grown by means of ECALE with different thicknesses and Cu/Sn ratio. The “ex situ” chemical and physical characterization carried out by means of SEM, XPS, PAR-XPS and TOF-SIMS has highlighted that the nominal stoichiometry is not respected and that the as prepared films are characterized by porous structures. In particular, the thinner deposit (sample #1), less than 10 nm thick, has large pores probably due to structural rearrangements. The homogeneity of the deposit improves upon increasing the number of deposition cycles, and

the band gap resulted reduced. For the first time the chemical composition of electrochemically grown copper–tin sufide layers has been fully investigated. It was found that the Cu/Sn ratio is not affected significantly by the number of cycles: copper was always the prevailing metal in the deposit. Accordingly, we propose that a cooperative effect between the CuS and Sn–S layers during ECALE is operating. On the one hand, SnS deposition is limited to an almost constant ratio; on the other hand the ECALE of SnS layers occurs to an high number of cycles, whereas this does not occur for the binary Sn_xS_y compound [51]. The synergic use of PAR-XPS and TOF-SIMS depth profiling proved to be a powerful tool for the investigation of electrochemically grown sulfide layers. This approach, coupled to the more conventional electrochemical techniques, enables the full understanding of the physical properties of the ECALE deposits, in order to design and optimize highly efficient cheap and green photovoltaic devices.

Finally, we want to stress that an optimized Cu/Sn ratio, as well as the production of pore free deposits will represent undemandable milestones in the the production of cost-effective absorber materials.

Acknowledgments

This work was partly supported by the Portugal Fundação para a Ciência e a Technologia (FCT) via the project PTDC/CTM-ENE/2514/2012. This study was developed with collaboration and financial assistance of Bluclad srl; Gabbrielli Technology. Regione Toscana is also acknowledged for funding FDB under two “Progetto mirato sulla Silice Libera Cristallina” programs.

References

[1] P. Bihouix, B. De Guillebon, Quel Futur Pour Les Métaux?, EDP Sciences, Paris, 2010 (in French).
[2] K. Jimbo, R. Kimura, T. Kamimura, S. Yamada, W.S. Maw, H. Araki, K. Oishi, H. Katagiri, Cu_2ZnSnS_4-type thin film solar cells using abundant materials, Thin Solid Films 515 (2007) 5997–5999.
[3] U. Bardi, The Limiths to Growth Revisited, first ed., Springer Verlag, New York, 2011.
[4] F. Di Benedetto, D. Borrini, A. Caneschi, G. Fornaciai, M. Innocenti, A. Lavacchi, C.A. Massa, G. Montegrossi, W. Oberhauser, L.A. Pardi, M. Romanelli, Magnetic properties and cation ordering of nanopowders of the synthetic analogue of kuramite, Cu_3SnS_4, Phys. Chem. Miner. 38 (2011) 483–490.
[5] I. Bencistà, F. Di Benedetto, M. Innocenti, A. De Luca, G. Fornaciai, A. Lavacchi, G. Montegrossi, W. Oberhauser, L.A. Pardi, M. Romanelli, F. Vizza, M.L. Foresti, Phase composition of CuXS thin films: spectroscopic evidence of covellite formation, Eur. J. Mineral. 24 (2012) 879–884.
[6] S. Schorr, Structural aspects of adamantine like multinary chalcogenides, Thin Solid Films 515 (2007) 5985–5991.
[7] F. Di Benedetto, T. Evstigneeva, M. Borgheresi, A. Caneschi, M. Romanelli, The unusual magnetic properties of kuramite–stannite pseudobinary series: a SQUID and EPR survey, Phys. Chem. Miner. 36 (2009) 301–309.
[8] Q. Chen, S. Cheng, S. Zhuang, X. Dou, Cu_2ZnSnS_4 solar cell prepared entirely by non-vacuum processes, Thin Solid Films 520 (2012) 6256–6261.
[9] D.B. Mitzi, O. Gunawan, T.K. Todorov, K. Wang, S. Guha, The path towards a high-performance solution-processed kesterite solar cell, Sol. Energy Mater. Sol. C 95 (2011) 1421–1436.
[10] S. Marchionna, P. Garattini, A. Le Donne, M. Acciarri, S. Tombolato, S. Binetti, Cu_2ZnSnS_4 solar cells grown by sulphursulfurisation of sputtered metal precursors, Thin Solid Films 542 (2013) 114–118.
[11] R.B.V. Chalapathy, G.S. Jung, B.T. Ahn, Fabrication of Cu_2ZnSnS_4 films by sulfurization of Cu/ZnSn/Cu precursor layers in sulfur atmosphere for solar cells, Sol. Energ. Mat. Sol. C. 95 (2011) 3216.
[12] S. Abermann, Non-vacuum processed next generation thin film photovoltaics: towards marketable efficiency and production of CZTS based solar cells, Sol. Energy 94 (2013) 37–70.
[13] A. Ennaoui, M. Lux-Steiner, A. Weber, D. Abou-Ras, I. Kötschau, H.W. Schock, R. Schurr, A. Hölzing, S. Jost, R. Hock, T. Voβ, J. Schulze, A. Kirbs, , Cu_2ZnSnS_4 thin film solar cells from electroplated precursors: novel low-cost perspective, Thin Solid Films 517 (2009) 2511–2514.
[14] J.J. Scragg, D.M. Berg, P.J. Dale, A 3.2% efficient Kesterite device from electrodeposited stacked elemental layers, J. Electroanal. Chem. 646 (2010) 52–59.
[15] D. Lincot, Electrodeposition of semiconductors, Thin Solid Films 487 (2005) 40.
[16] B.W. Gregory, J.L. Stickney, Electrochemical atomic layer epitaxy (ECALE), J. Electroanal. Chem. 300 (1991) 543–561.
[17] M.L. Foresti, G. Pezzatini, M. Cavallini, G. Aloisi, M. Innocenti, R. Guidelli, Electrochemical atomic layer epitaxy deposition of CdS on Ag(111): an electrochemical and STM investigation, J. Phys. Chem. B 102 (1998) 7413–7420.
[18] M. Innocenti, G. Pezzatini, F. Forni, M.L. Foresti, CdS and ZnS deposition on Ag (111) by electrochemical atomic layer epitaxy, J. Electrochem. Soc. 148 (2001) C357–C362.
[19] F. Loglio, M. Innocenti, A. Jarek, S. Caporali, I. Pasquini, M.L. Foresti, Nickel sulfur thin films deposited by ECALE: electrochemical, XPS and AFM characterization, J. Electroanal. Chem. 638 (2010) 15–20.
[20] I. Şişman, Ü. Demir, Electrochemical growth and characterization of size-quantized CdTe thin films grown by underpotential deposition, J. Electroanal. Chem. 651 (2011) 222–227.
[21] M. Innocenti, F. Forni, G. Pezzatini, R. Raiteri, F. Loglio, M.L. Foresti, Electrochemical behavior of As on silver single crystals and experimental conditions for InAs growth by ECALE, J. Electroanal. Chem. 514 (2012) 75–82.
[22] F. Loglio, A.M. Telford, E. Salvietti, M. Innocenti, G. Pezzatini, S. Cammelli, F. D'Acapito, R. Felici, A. Pozzi, M.L. Foresti, Ternary $Cd_xZn_{1-x}Se$ deposited on Ag (1 1 1) by ECALE: electrochemical and EXAFS characterization, Electrochim. Acta 53 (2008) 6978.
[23] F. Loglio, M. Innocenti, G. Pezzatini, M.L. Foresti, Ternary cadmium and zinc sulfides and selenides: electrodeposition by ECALE and electrochemical characterization, J. Electroanal. Chem. 562 (2004) 117–125.
[24] M.L. Foresti, S. Milani, F. Loglio, M. Innocenti, G. Pezzatini, S. Cattarin, Ternary CdS_xSe_{1-x} deposited on Ag(111) by ECALE: synthesis and characterization, Langmuir 21 (2005) 6900–6907.
[25] J. Li, L. Jiang, B. Wang, F. Liu, J. Yang, D. Tang, Y. Lai, J. Li, Electrodeposition and characterization of copper bismuth selenide semiconductor thin films, Electrochim. Acta 87 (2013) 153–157.
[26] F. Di Benedetto, I. Bencistà, S. Caporali, S. Cinotti, A. De Luca, A. Lavacchi, F. Vizza, M. Muniz Miranda, M.L. Foresti, M. Innocenti, Electrodeposition of ternary $Cu_xSn_yS_z$ thin films for photovoltaic applications, Prog. Photovolt. 22 (2014) 97–106.
[27] C.A.A. Ghumman, A.M.C. Moutinho, A. Santos, O.M.N.D. Teodoro, A. Tolstogouzov, An upgraded TOF-SIMS VG Ionex IX23LS: study on the negative secondary ion emission of III–V compound semiconductors with prior neutral cesium deposition, Appl. Surf. Sci. 258 (2012) 2490–2497.
[28] C.A.A. Ghumman, A.M.C. Moutinho, A. Santos, A. Tolstogouzov, O.M.N. D. Teodoro, TOF-SIMS VG Ionex IX23LS: upgrade and application for the urinary stones analysis, Surf. Interface Anal. 45 (2013) 532–536.
[29] M.C. Biesinger, L.W.M. Lau, A.R. Gerson, R.S.C. Smart, Resolving surface chemical states in XPS analysis of first row transition metals, oxides and hydroxides: Sc, Ti, V, Cu and Zn, Appl. Surf. Sci. 257 (2010) 887–898.
[30] D. Perry, J.A. Taylor, X-ray photoelectron and Auger spectroscopic studies of Cu_2S and CuS, J. Mater. Sci. Lett. 5 (1986) 384–386.
[31] G. Schön, High resolution Auger electron spectroscopy of metallic copper, J. Electron Spectrosc. Relat. Phenom. 1 (1972) 377–387.
[32] S.P. Kowalczyk, R.A. Pollak, F.R. McFeely, L. Ley, D.A. Shirley, $L_{2,3}M_{45}M_{45}$ Auger spectra of metallic copper and zinc: theory and experiment, Phys. Rev. B 8 (1973) 2387–2391.
[33] E.D. Roberts, P. Weightman, C.E. Johnson, Auger vacancy satellite structure in the $L_3M_{4,5}M_{4,5}$ Auger spectra of copper, J. Phys. C Solid State Phys. 8 (1975) L301.
[34] E. Antonides, E.C. Janse, G.A. Sawatzky, LMM Auger spectra of Cu, Zn, Ga, and Ge. I. Transition probabilities, term splittings, and effective Coulomb interaction, Phys. Rev. B 15 (1977) 1669–1679.
[35] E. Antonides, E.C. Janse, G.A. Sawatzky, LMM Auger spectra of Cu, Zn, Ga, and Ge, II. Relationship with the L23 photoelectron spectra via the $L_2L_3M_{45}$ Coster-Kronig process, Phys. Rev. B 15 (1977) 4596–4601.
[36] National Institute of Standards and Technology, “XPS Database,” (⟨http://srdata.nist.gov/xps⟩, 2012, last access on September the 4.09.14).
[37] S.W. Gaarenstroom, N. Winograd, Initial and final state effects in the ESCA spectra of cadmium and silver oxides, J. Chem. Phys. 67 (1977) 3500–3506.
[38] J.F. Moulder, W.F. Stickle, P.E. Sobol, K.D. Bomben, Handbook of X-ray Photoelectron Spectroscopy, in: J. Chastain (Ed.), Perkin–Elmer Corporation, Minnesota, 1992.
[39] M. Cruz, J. Morales, J.P. Espinos, J. Sanz, XRD, XPS and ^{119}Sn NMR study of tin sulfides obtained by using chemical vapor transport methods, J. Solid State Chem. 175 (2003) 359–365.
[40] F. Loglio, A.M. Telford, E. Salvietti, M. Innocenti, G. Pezzatini, S. Cammelli, F. D'Acapito, R. Felici, A. Pozzi, M.L. Foresti, Ternary $Cd_xZn_{1-x}Se$ nanocrystals deposited on Ag(111) by ECALE: AFM and EXAFS characterization, Electrochim. Acta 53 (2008) 6978–6987.
[41] S. Fiechter, M. Martinez, G. Schmidt, W. Henrion, Y. Tomm, Phase relations and optical properties of semiconducting ternary sulfides in the system Cu–Sn–S, J. Phys. Chem. Solids 64 (2003) 1859–1862.
[42] V.R. Deline, W. Katz, C.A. Evans, P. Williams, Mechanism of the SIMS matrix effect, Appl. Phys. Lett. 33 (1978) 832–835.
[43] R.G. Wilson, SIMS quantification in Si, GaAs, and diamond-an update, Int. J. Mass Spectrom. Ion Process. 143 (1995) 43–49.
[44] L.L. Cheng, L.H. Liu, M.X. Wang, S.C. Wang, G.D. Wang, Q.Y. Zhou, Q.Z. Chen, Preparation of SnS films using solid sources deposited by the PECVD method with controllable film characters, J. Alloy. Compd. 545 (2012) 122–129.

[45] G. Liu, T. Schulmeyer, J. Brötz, A. Klein, W. Jaegermann, Interface properties and band alignment of Cu_2S/CdS thin film solar cells, Thin Solid Films 431–432 (2003) 477–482.
[46] Y. Rodriguez-Lazcano, H. Martinez, M. Calixto-Rodriguez, A. Nuñez Rodriguez, Properties of CuS thin films treated in air plasma, Thin Solid Films 517 (2009) 5951–5955.
[47] Y.-T. Lin, J.-B. Shi, Y.-C. Chen, C.-J. Chen, P.-F. Wu, Synthesis and characterization of tin disulfide (SnS_2) nanowires, Nanoscale Res. Lett. 4 (2009) 694 –69.
[48] H. Guan, H. Shen, C. Gao, X. He, The influence of annealing atmosphere on the phase formation of Cu–Sn–S ternary compound by SILAR method, J. Mater. Sci: Mater. Electron. 24 (2013) 3195–3198.
[49] K.H.L. Zhang, V.K. Lazarov, T.D. Veal, F.E. Oropeza, C.F. McConville, R.G. Egdell, A. Walsh, Thickness dependence of the strain, band gap and transport properties of epitaxial In_2O_3 thin films grown on Y-stabilised ZrO_2(111), J. Phys.-Condens. Matter 23 (2011) 334211.
[50] M. Pandiaraman, N. Soundarajan, C. Vijayan, Effect of thickness on the optical band gap of silver telluride thin films, J. Ovonic Res. 7 (2011) 21–29.
[51] M. Innocenti, I. Bencistà, F. Di Benedetto, S. Cinotti, A. De Luca, S. Bellandi, A. Lavacchi, M. Muniz Miranda, F. Vizza, F. Marinelli, L. Dei, E. Carretti, C. Zafferoni, M.L. Foresti, Underpotential deposition of Sn on S-covered Ag (111), ECS Trans. 50 (2013) 1–7.